Poisson's ratio in the lower mantle beneath Alaska: Evidence for compositional heterogeneity

Rebecca L. Saltzer[1]

Department of Earth, Atmospheric and Planetary Sciences, Massachusetts Institute of Technology, Cambridge, Massachusetts, USA

Eléonore Stutzmann

Institut Physique du Globe, Paris, France

Robert D. van der Hilst

Department of Earth, Atmospheric and Planetary Sciences, Massachusetts Institute of Technology, Cambridge, Massachusetts, USA

Received 31 July 2003; revised 28 January 2004; accepted 24 February 2004; published 9 June 2004.

[1] Using waveform cross correlation, we have measured ~17,000 *P* and *S* wave differential travel times from earthquakes and receivers near a great circle path from Japan, across Alaska, to North America. We jointly invert the data for variations in shear and bulk sound speed and derived Poisson's ratio variations in the mantle beneath 1000 km depth. We explore the model space using different levels of regularization and our conclusions are based on a range of models that give acceptable data fits. The correlation between v_S and v_P variations is good to ~1500 km depth but gradually degrades in the bottom 1000 km, whereas the ratio $R = \partial \ln v_S / \partial \ln v_P$ is between 1.0 and 1.8 at most depths. Our data suggest that there is no significant correlation between bulk and shear wave speed, but they appear anticorrelated in several regions. We estimate the effect on the Poisson's ratio of changes in temperature, iron content, and the magnesiowüstite (mw) to perovskite (pv) ratio. At all depths the effect of temperature is largest and that of the pv to mw ratio smallest. Our data cannot resolve the trade-off between thermal and compositional effects, but explaining the Poisson's ratio variability by temperature alone would require unrealistic perturbations and it would not explain the inferred anticorrelation between shear and bulk sound speed. Our results suggest that despite *R* being significantly smaller than 2.5 we need a combination of thermal and compositional effects in order to explain the elastic parameter variations in the deep mantle beneath Alaska, with realistic values of ΔT of ~300–800 K, variation in X_{Fe} of ~4%, and pv enrichment (or depletion) of up to ~10% just sufficient for explaining the data. *INDEX TERMS:* 7207 Seismology: Core and mantle; 8124 Tectonophysics: Earth's interior—composition and state (1212); 8180 Tectonophysics: Tomography; *KEYWORDS:* Poisson's ratio, tomography, composition

Citation: Saltzer, R. L., E. Stutzmann, and R. D. van der Hilst (2004), Poisson's ratio in the lower mantle beneath Alaska: Evidence for compositional heterogeneity, *J. Geophys. Res.*, *109*, B06301, doi:10.1029/2003JB002712.

1. Introduction

[2] The major element mineralogy and phase chemistry of the lower mantle is central to many discussions about mantle convection and Earth's evolution over geological time. There is growing consensus on its bulk composition, and it is thought that much of the spherically averaged estimates of elastic parameters (such as wave speed and wave speed ratios), as represented in reference Earth models such as PREM [*Dziewonski and Anderson*, 1981], reflects the increase of temperature and pressure with depth, except, perhaps, in the deepest 300–500 km of the mantle [e.g., *Garnero*, 2000; *Masters et al.*, 2000; *Ritsema and van Heijst*, 2002; *Antolik et al.*, 2003]. However, the level and nature of aspherical variations in composition and, indeed, the very existence of chemically distinct domains in the lower mantle have remained enigmatic. Geochemical data and heat flow considerations both suggest that the mantle is chemically heterogeneous [e.g., *Zindler and Hart*, 1986; *Hofmann*, 1997], but there is strong geophysical evidence against compositional stratification of the mantle, at least at 660 km depth (for a recent review, see *Albarède and van der Hilst* [2002]). In efforts to reconcile these views, several investigators have proposed that lateral variations in composition might exist either as

[1]Now at ExxonMobil, Houston, Texas, USA.

0148-0227/04/2003JB002712$09.00

distinct domains, blobs, or piles in the deep mantle [e.g., *Tackley*, 1998; *Becker et al.*, 1999; *Davaille*, 1999; *Kellogg et al.*, 1999; *van der Hilst and Kárason*, 1999; *Anderson*, 2002], as diffuse regions of incompletely mixed material [e.g., *Helffrich and Wood*, 2001], or a combination of both [e.g., *Coltice and Ricard*, 1999], while others argue that the geochemical noble gas and trace element record can be explained with time-dependent convection without a need for compositionally distinct ''reservoirs'' [e.g., *Davis*, 2002].

[3] To some extent the onus is on seismic imaging to provide robust evidence for changes in (major element) composition, at least on the spatial scales that can be detected by the seismic waves used. This has remained a major challenge, however. The seismological evidence for the existence of compositionally distinct domains has long been equivocal, but there are an increasing number of observations that cannot readily be explained by changes in temperature and pressure alone [e.g., *van der Hilst and Kárason*, 1999]. Globally, for example, the patterns of *P* and *S* wave heterogeneity are strongly correlated down to ~2000 km depth, but below that depth the correlation declines [*Robertson and Woodhouse*, 1996; *Grand et al.*, 1997]. At those same depths, the bulk (κ) and shear (μ) moduli begin to behave differently from one another [*Su and Dziewonski*, 1997; *Kennett et al.*, 1998; *Masters et al.*, 2000], and *Forte and Mitrovika* [2001] and *Forte et al* [2002] have shown that bulk sound velocity anomalies are strongly correlated to composition perturbations, whereas shear velocity anomalies are strongly anticorrelated to temperature variations. Toward the base of the mantle the spherically averaged ratio of relative perturbation in v_S and v_P, often expressed as $R = R(z) = \partial \ln v_S / \partial \ln v_P$, is higher than values that would be expected from thermal variations alone [e.g., *Masters et al.*, 2000; *Romanowicz*, 2001]. The *R* value that unambiguously points to compositional effects is still debated and may be influenced by anelasticity, but mineral physicists seem to concur that values of up to 1.8 at 1500 km depth, 2.0 at 2000 km, and 2.3 in the deepest mantle can still be attributed to temperature and pressure affects, with higher values requiring other explanations (J. Brodholt et al., Fréjus Workshop, personal communication, 2003). It should be noted, however, as we will demonstrate here, that laterally averaged values of *R* smaller than this do not rule out compositional heterogeneity. Studies that consider three-dimensional (3-D) heterogeneities confirm that the lateral variation in *R* is most pronounced, and the values of *R* are most extreme, near the base of the mantle. However, they also find that high *R* values can occur as far as 1000 km above the core-mantle boundary (CMB) in regions away from deep subduction, that is, in deep mantle regions where also the lowest wave speeds are detected, whereas *R* maintains moderate values ($R < 2$) elsewhere [*Masters et al.*, 2000; *Saltzer et al.*, 2001]. *Saltzer et al.* [2001], among others, show that away from major downwellings the depth range of high *R* values is also marked by a negative correlation of variations in bulk and shear speed. Furthermore, joint inversions of free oscillation and gravity data suggest high densities in the lower mantle associated with low-velocity upwellings [*Ishii and Tromp*, 1999, 2001], although the robustness of this inference is still debated [e.g., *Resovsky and Ritzwoller*, 1999; *Romanowicz*, 2001]. While consistent with compositional heterogeneity, none of these studies proves unequivocally the existence, let alone constrains the nature, of compositionally distinct mantle domains.

[4] There are, at least, two major difficulties with seismological studies of compositional heterogeneity that rely on wave speed ratios. First, without absolute values the trade-off between temperature and compositional effects cannot be resolved, so that the interpretation in terms of the origin of the wave speed perturbations remains nonunique. Second, inferring variations in bulk sound speed or determining wave speed ratios should only be done in regions were the constraints on *P* wave speed are as good as that of *S*. In global inversions this may pose a major problem, since not only is data coverage uneven, it is also different for *P*- and *S*-type data. For instance, in many regions, upper mantle shear wave speed is best constrained by surface waves, which are, however, not very sensitive to changes in v_P. Depending on the databases used, the sampling differences can be compounded by differences in quality of *P* and *S* data [e.g., *Grand et al.*, 1997].

[5] In contrast to previous deep mantle studies of v_S/v_P, we do not draw inferences from global inversions but focus on a region with particularly dense coverage of sources and receivers. The great circle corridor from Japan, across Alaska, and to western North America lies along continental or island arc plate boundaries with a fairly continuous distribution of earthquakes and stations (Figure 1). The large number of crossing paths produced by this source-receiver distribution is used to determine wave speed ratios in the entire depth range of the mantle, but we only focus on the lower mantle beneath ~1000 km depth where resolution is best. Global *P* and *S* wave tomography [e.g., *van der Hilst et al.*, 1997; *Grand et al.*, 1997; *Kárason and van der Hilst*, 2001] suggests that remnants of subducted slab may be present in the deep mantle beneath Canada and easternmost North America, but there is no evidence for deep subduction directly beneath the central part of our study region. Previous studies suggested that the lowermost mantle beneath the region under study is fast for *S* waves but relatively slow for *P* [*Wysession et al.*, 1992; *van der Hilst et al.*, 1997; *Grand et al.*, 1997; *Li and Romanowicz*, 1996; *Masters et al.*, 1996; *Bijwaard et al.*, 1998; *Kárason and van der Hilst*, 2001; *Ritsema and van Heijst*, 2002], which is difficult to explain by thermal variations alone. In addition, there is both evidence for [*Revenaugh and Meyer*, 1997; *Garnero and Helmberger*, 1998] and against [*Castle and van der Hilst*, 2000; *Persh et al.*, 2001] an ultralow-velocity zone at the CMB directly beneath and to the south of Aleutians.

[6] Following *Robertson and Woodhouse* [1996], *Kennett et al.* [1998], and *Saltzer et al.* [2001], we force the *P* and *S* sampling (and, ultimately, model resolution) to be as similar as possible by using data only when both the *P* and *S* arrivals for a given source-receiver pair can be measured. We determine differential travel time residuals by cross correlation on broadband waveforms. Using a large number of data that are carefully selected by visual inspection, we determine the variation of *R* and the range of Poisson's ratio as a function of depth beneath this region and investigate to what extent these results can be explained by a thermal origin or by variations in composition (that is,

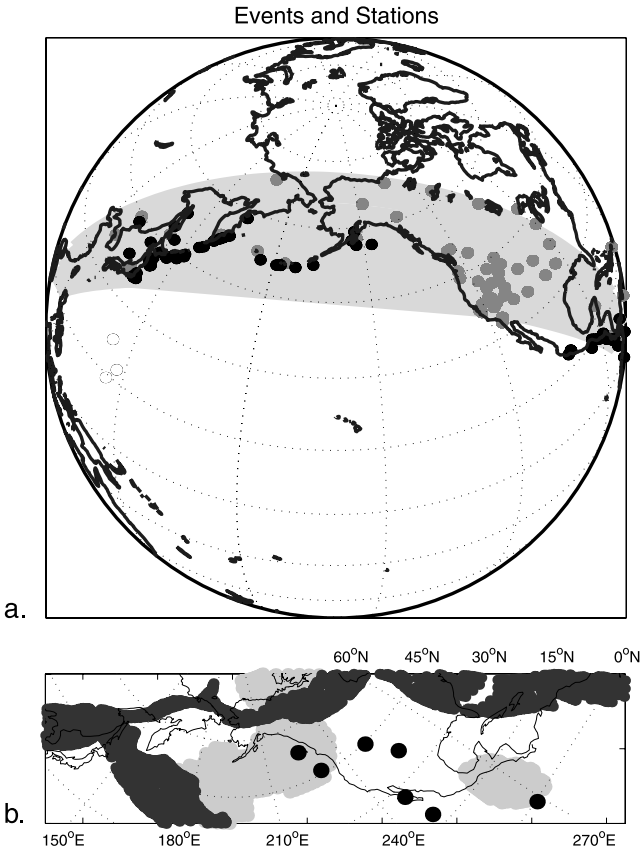

Figure 1. (a) Location map of earthquakes (black circles) and stations (gray circles). Shaded gray region shows the width of the corridor investigated. (b) Corridor investigated. Dashed lines show parallels and meridians for geographical correspondence. Locations of ultralow-velocity zones are those reported in previous studies (light gray) [e.g., *Revenaugh and Meyer*, 1997; *Garnero and Helmberger*, 1998], inferred locations of slabs (dark gray) >90 Myr old from plate reconstructions [*Steinberger*, 2000], and the surface projection of hot spots at the core-mantle boundary (black circles) [*Richards et al.*, 1988].

iron content and proportionality between perovskite and magnesiowüstite).

2. Data

[7] In our study we consider direct arrivals (*P*, *S*) and core reflections (*PcP*, *ScS*). The data were obtained from GEOSCOPE and Incorporated Research Institutions for Seismology (IRIS) and comprised 76 stations and 128 large events ($m_b > 5.8$) with origin times between 1993 and 2000 that occurred anywhere along the corridor of interest. At the expense of some spatial resolution, events outside of this corridor were excluded in order to avoid the erroneous mapping of structure from outside the plane. To ensure comparable sampling for the *P* and *S* type data, we have selected data only if both the *P* (or *PcP*) and *S* (or *ScS*) could be measured at the same station. The advantage of this approach is that we compare regions that are similarly sampled by both wave types, and therefore the sensitivity matrices and the effects of regularization (see section 3) are nearly identical for the *P* and *S* models. We remark, however, that even with this selection of *P* and *S* pairs, the difference in bottom point between the *P* and *S* paths can be considerable (for model ak135 it is ~200 km for the largest epicentral distances considered).

[8] We measured differential travel times using waveform cross correlation on unfiltered, broadband seismograms (Figure 2). We selected a reference station on which we manually picked the first swing of the direct *P* phase (and *S*). This signal was then cross-correlated with a time window comprising a few seconds of noise followed by the arrival of the direct phase at the other stations that recorded the same event. The direct arrivals were then shifted according to their measured differential time, $P1-P2$ (or $S1-S2$). We visually inspected them together with the cross correlations (Figures 2a and 2b), and noisy traces were discarded. Harvard's centroid moment tensor database was used to check the polarity of a given seismogram. The $P1-P2$ and $S1-S2$ differential travel times were measured on the vertical and transverse component, respectively.

[9] The dominant period of the broadband data is ~1 s for *P* and ~4 s for the *S* waves, but by correlating the first swing of the phase arrivals on unfiltered broadband data we tend to measure the high-frequency part of each waveform. We did not determine the reading error for individual measurements, but from visual inspection we estimate the standard error to be $\sim 0.4-0.5$ s for *P* wave picks and $\sim 0.8-1.0$ s for *S*. These values are used to calculate χ^2 when we construct the models for Poisson's ratio.

[10] We use differential travel times because they are less sensitive to errors in source location and origin. The differential travel times are compared to predictions from a 1-D reference Earth model, here ak135 [*Kennett et al.*, 1995], in order to calculate differential travel time residuals. These residuals are then corrected for Earth's ellipticity [*Kennett and Gudmundsson*, 1996].

[11] In addition to direct phases we also measured *PcP-P* and *ScS-S* differential travel times for individual source-receiver pairs (Figures 2c and 2d) on vertical and transverse component, respectively. Before cross correlating the first swing of the *P* (*S*) waveform with the *PcP* (*ScS*) arrival we used a *t** operator [e.g., *Aki and Richards*, 1980] to account for differences in attenuation along the ray paths. Unfortunately, there are many events that excited beautiful *ScS* but no discernible *PcP*, and with our conservative approach such events could not be used for further analysis.

[12] Our final data set consists of 16,728 relative *P* and *S* travel time residuals and 198 matched pairs of *PcP-P* and *ScS-S* measurements (99 for each core phase). The source-receiver combinations produced a large number of crossing rays in the deep mantle beneath the corridor under study (Figure 3).

3. Methodology

3.1. Inversion

[13] Parameters such as the Poisson's ratio and bulk sound speed can either be inferred from shear and compressional wave speed or be solved directly. In the first approach, the following formulation can be used to obtain

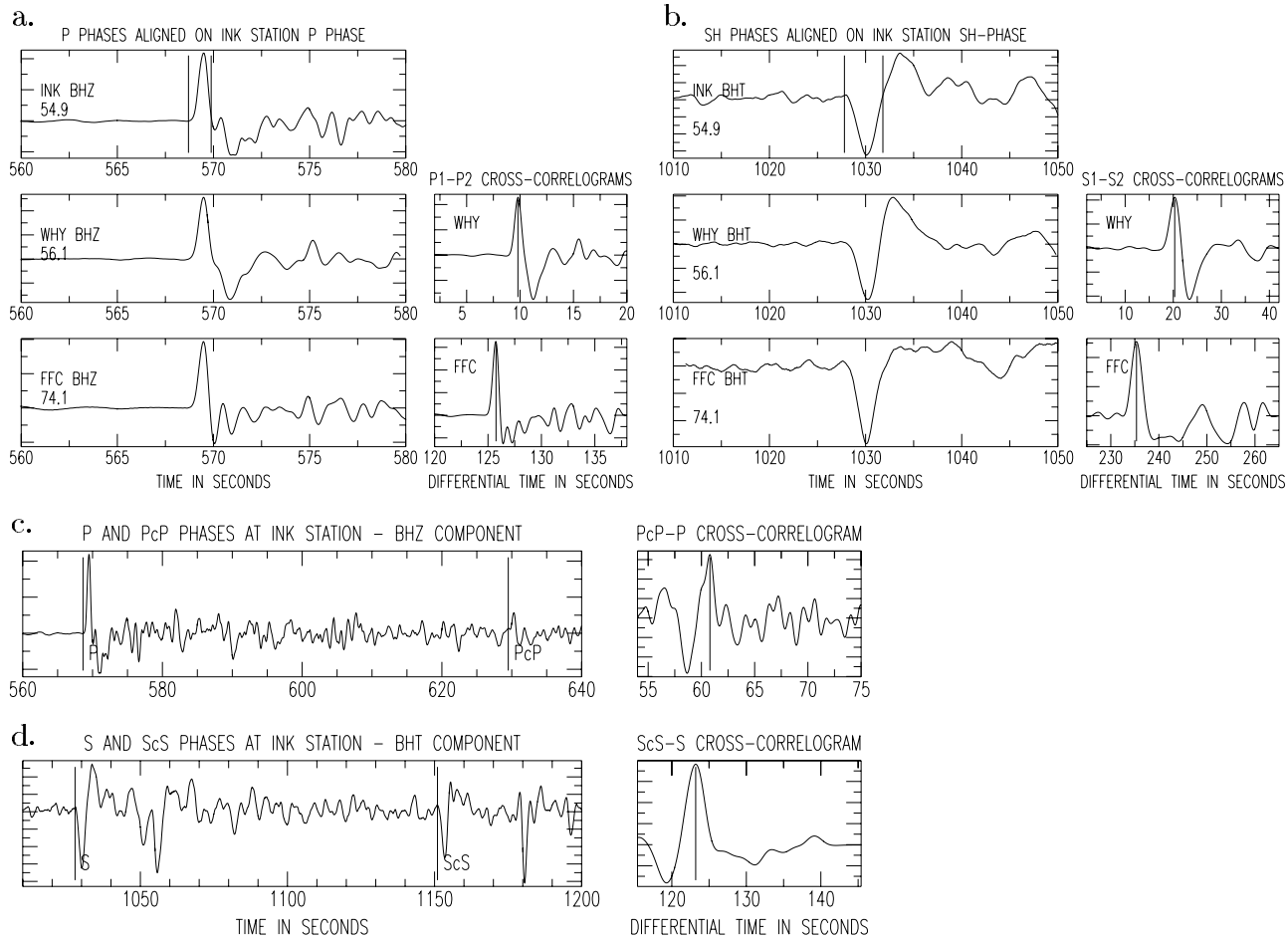

Figure 2. Example of data for an event on 20 July 2000 (latitude 36.4°N, longitude 141.16°E, depth 46 km, m_b = 6.1). (a) $P1-P2$ differential travel time measurement using vertical components (BHZ). P wave is plotted for the reference station (top trace, station INK), and two other stations that have recorded the same event (middle and bottom left figures, stations WHY and FFC). Epicentral distance is written on each plot. The P wave first lobe of the reference trace, that is, the signal between the two vertical lines in the top plot, is cross-correlated with a window that contains P wave at the other stations. The differential travel time corresponds to the cross-correlogram maximum (vertical line on the cross-correlogram middle and bottom right plots). It is used for shifting data so that they get aligned to the reference station P wave for visual inspection. (b) $S1-S2$ differential travel time measurement; same as Figure 2a but for S wave on transverse component (BHT). (c) *PcP-P* differential travel time measurement. The vertical seismogram (BHZ) is plotted on the left plot. The P wave first lobe is selected, modified using a t^* operator to account for differences in attenuation along the ray paths and cross-correlated with a window that contains the *PcP* phase. Differential travel time corresponds to cross-correlogram maximum (vertical line on the right plot), and it is reported on the seismogram with label *PcP*. (d) *ScS-S* differential travel time measurement; same as Figure 2c but for S wave on transverse components (BHT).

tomographic images of variations in P and S wave speed by joint inversion of P and S wave data:

$$\begin{matrix} \mathbf{G} & & \mathbf{m} & = & \mathbf{d} \end{matrix}$$

$$\begin{bmatrix} P-\text{matrix} & 0 \\ 0 & S-\text{matrix} \end{bmatrix} \begin{bmatrix} P \\ S \end{bmatrix} = \begin{bmatrix} \delta t_p \\ \delta t_s \end{bmatrix}. \quad (1)$$

The matrix **G**, which represents the sampling used for the back projection of the data, contains the partial derivatives that represent the functional dependence of the travel time residuals to the slowness perturbations, **m** is the slowness perturbation model vector, and **d** is the vector of measured differential travel time residuals. In this lower mantle study we ignore anisotropy. For an isotropic medium the bulk sound wave speed, v_ϕ, can be derived from v_P and v_S according to

$$v_\phi^2 = \frac{\kappa}{\rho} = v_p^2 - \frac{4}{3}v_s^2. \quad (2)$$

The bulk sound wave speed depends only on bulk modulus (κ) and density (ρ), so that in combination with shear wave speed, the separate effects of the bulk and shear moduli can be evaluated. In addition, the bulk sound wave speed can be compared directly with experimental and theoretical mineral physics results and is relatively insensitive to anelastic effects.

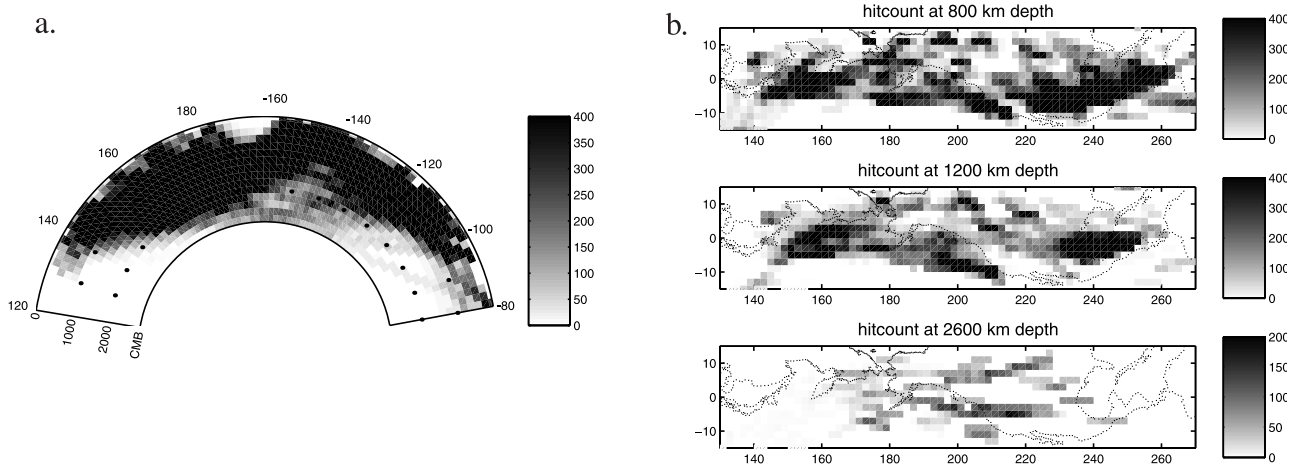

Figure 3. Hit count (a) for number of times a ray passes through each cell of the tomographic model along a cross section and (b) for three depths 800, 1200, and 2600 km. Since the source-receiver geometry for the *P* and *S* waves is the same, the hit count pattern looks the same for both as well.

[14] In the second approach one obtains bulk sound and shear wave speed models directly from joint inversion of *P* and *S* wave data, using

$$\begin{bmatrix} \text{bulk1} - \text{matrix} & S1 - \text{matrix} \\ 0 & S2 - \text{matrix} \end{bmatrix} \begin{bmatrix} \phi \\ S \end{bmatrix} = \begin{bmatrix} \delta t_p \\ \delta t_s \end{bmatrix}. \quad (3)$$

The partial derivatives representing the dependence of the *P* wave travel time on variations in bulk sound and shear slowness perturbation, which constitute the bulk matrix, are obtained by rewriting equation (2) in terms of slowness and then taking the appropriate derivatives:

$$\delta t_p = \int_{ray} ds \delta a = \int_{ray} ds \left(\frac{a^3}{c^3} \delta c + \frac{4a^3}{3b^3} \delta b \right), \quad (4)$$

where $a = v_P^{-1}$, $b = v_S^{-1}$, $c = v_\phi^{-1}$, δt_P is the *P* wave travel time residual and δa, δb, and δc are the perturbations in *P* wave, *S* wave, and bulk sound slowness, respectively.

[15] From the results of the *P* and *S* inversions we can calculate the Poisson's ratio (σ):

$$\sigma = \frac{1}{2} \left\{ 1 - \left[\left(\frac{v_P}{v_S} \right)^2 - 1 \right]^{-1} \right\} = \frac{\lambda}{2(\lambda + \mu)}, \quad (5)$$

where λ and μ are the Lamé parameters (μ is rigidity, as before; $\lambda = \kappa + 2/3\mu$, κ is incompressibility).

[16] For the parameterization of the model space we used a regular grid of $2^\circ \times 2^\circ \times 200$ km constant velocity blocks, which is aligned along the great circle corridor that contains the majority of the sources and the receivers considered in our study. To determine the sensitivity matrix **G**, we traced rays through the radially stratified (i.e., 1-D) reference Earth model ak135 [*Kennett et al.*, 1995]. We ignore finite frequency wave propagation effects [e.g., *Dahlen et al.*, 2000] and use geometrical ray theory for both types of data, which is partly justified by the use of unfiltered broadband data and the observational practice of emphasizing the correlation of the first (high frequency) swing of the phase arrival instead of the entire waveform.

[17] We use hypocenter information from *Engdahl et al.* [1998]. The differential times are relatively insensitive to errors in source location and origin time, but owing to the difference in takeoff angle of the phases combined in the differential time, such as *P* and *PcP*, effects on source mislocation could map into our data. We account for such effects by adding relocation parameters for the different data types to model vector **m** and associated sensitivities to **G**. Upon inversion, all events moved less than 10 km and most moved only 1 or 2 km in any direction.

[18] As is the case for most other tomographic studies, the inversion problem is ill-posed in the sense that not all model parameters can be resolved independently. Moreover, the system of equations may be inconsistent owing to noise in the data. As a result, there is no unique solution. To select the range of acceptable models, we use a combination of two types of regularization. First, we use norm damping, which restricts the model variance and biases the value of the model parameters to that of the reference model. Second, we use gradient damping, which penalizes large differences between values in adjacent cells and thus acts as a smoothness criterion. The penalty function to be minimized thus takes the following form: $\|\mathbf{Gm} - \mathbf{d}\|^2 + \lambda_1 \|\mathbf{m}\|^2 + \lambda_2 \|\mathbf{Lm}\|^2 = \min$, with **L** the gradient operator and λ_1 and λ_2 control parameters to weight the relative importance of the norm damping and gradient damping, respectively; we used different values for horizontal and vertical gradient damping.

[19] We used LSQR, an iterative, conjugate gradient algorithm [*Paige and Saunders*, 1982; *Nolet*, 1985], to solve the systems of equations represented by equations (1) and (3). While remaining somewhat ad hoc, the level of regularization (that is, λ_1 and λ_2) was determined by means of a series of χ^2 tests with real and synthetic data. All tomographic models presented here were obtained after

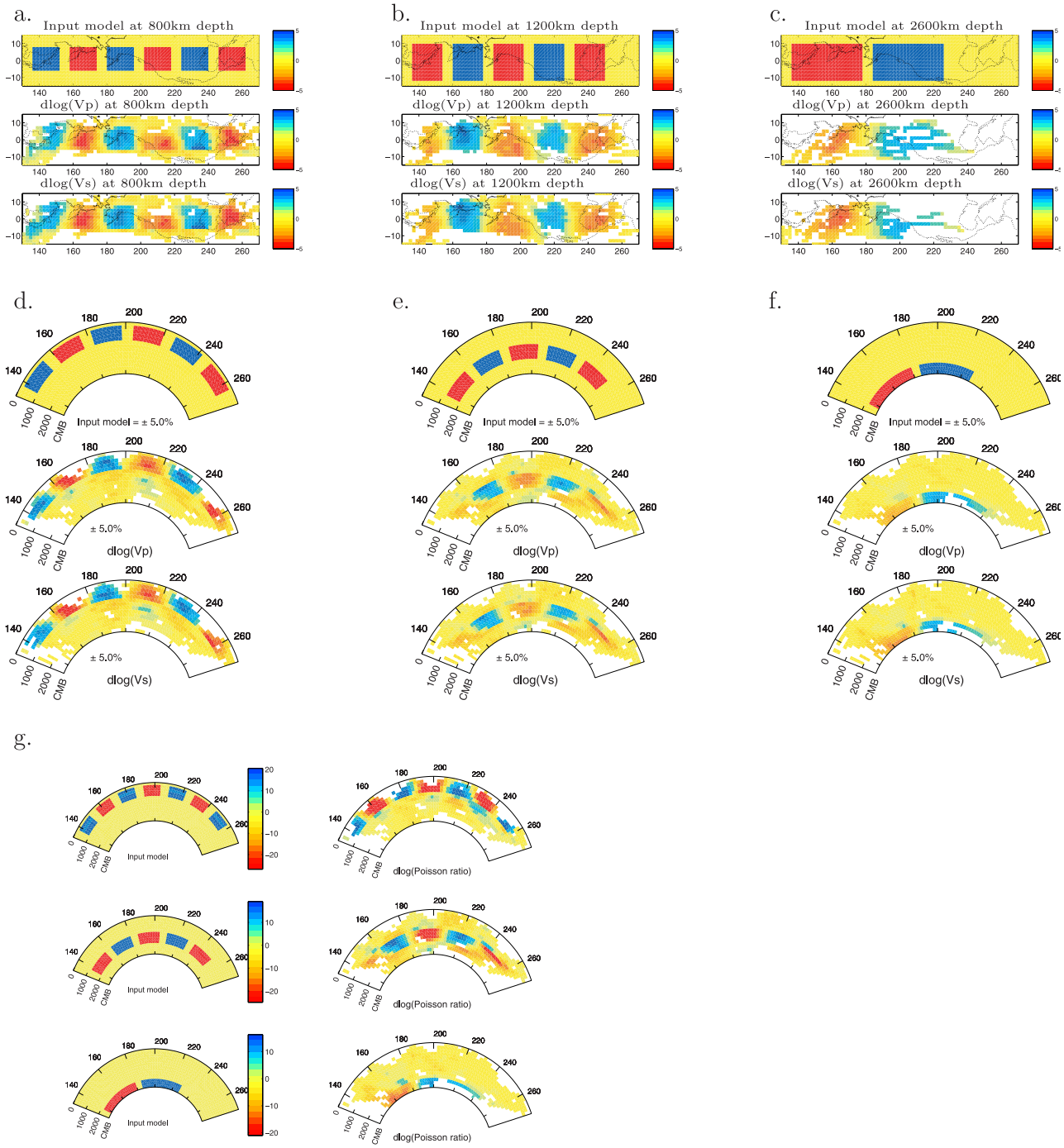

Figure 4. (a–f) Results of three synthetic tests in which the target anomalies are located in the upper (Figures 4a and 4d), the middle (Figures 4b and 4e), and the lower mantle (Figures 4c and 4f). Rays are traced through a known velocity model (top plots), and then the resulting travel time anomalies are jointly inverted to see what structure is actually recovered for the *P* wave model (middle plots) and *S* wave model (bottom plots). Models are plotted at given depths within the perturbed layer (800 km, Figure 4a; 1200 km, Figure 4b; 2700 km, Figure 4c) and along cross section at the center of the area of interest (Figures 4d, 4e, and 4f). Although the anomalies appear to increase in size with depth, in fact, they all have similar area when measured on a constant length scale such as kilometers. This exaggeration is a natural consequence of plotting our results on a constant angular degree scale. The color scale is the same for all plots between 5% and −5%. Cells that are not resolved (no ray passes through them) are left white. (g) Same as Figures 4d–4f but for Poisson's ratio perturbation. The input anomaly geometry is the same as in Figures 4d–4f, but with opposite sign (±5%) for *P* wave and *S* wave perturbations. The three input model cross sections are plotted on the left and the Poisson's ratio perturbations after inversion are plotted on the right.

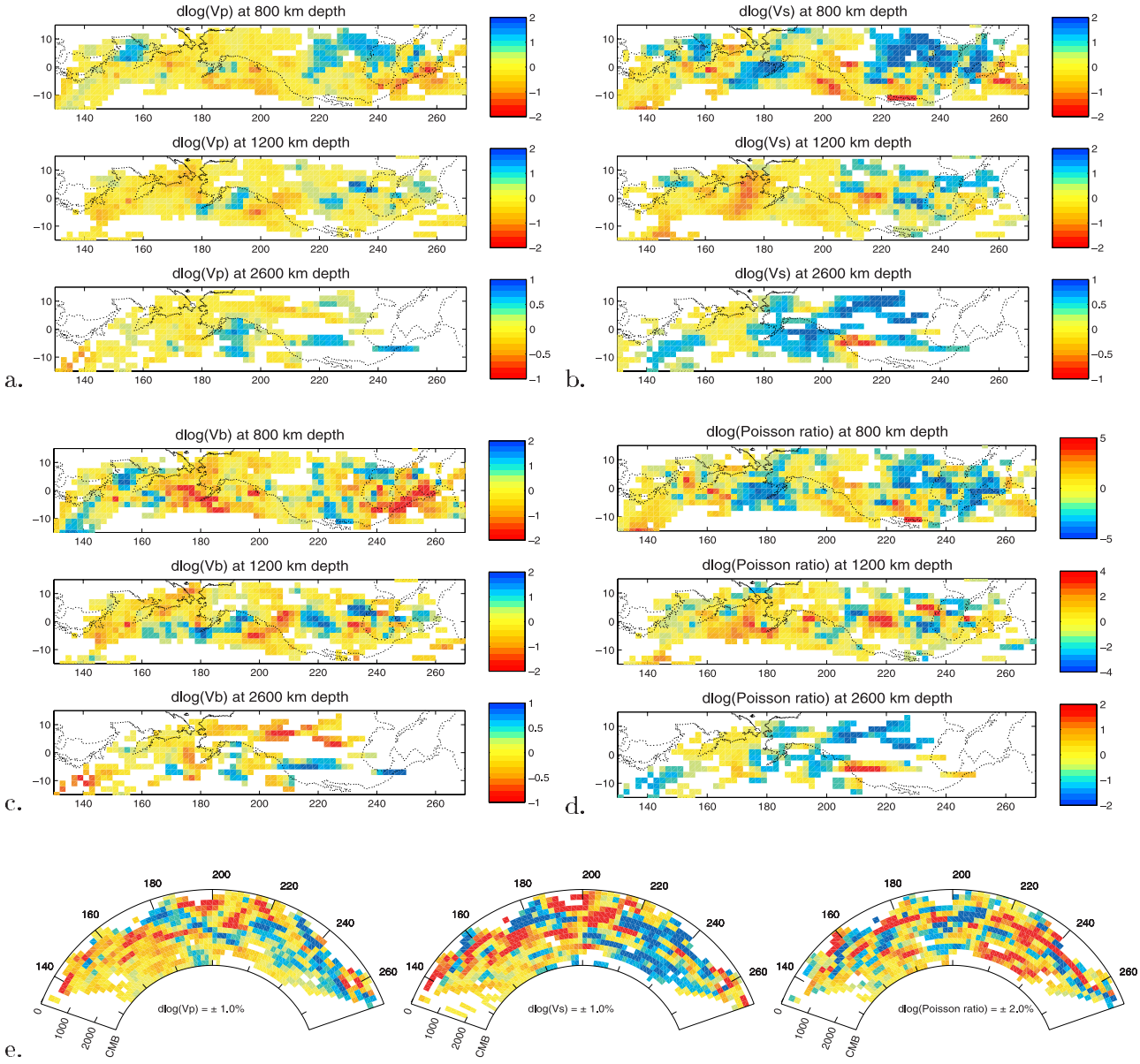

Figure 5. (a) *P* wave, (b) *S* wave, (c) bulk sound speeds, and (d) Poisson's ratio perturbations for one of the acceptable models at three depth 800, 1200, and 2600 km. Cells that are not resolved (no ray passes through them) are left white. (e) Cross section at the center of the model for *P* wave (left), *S* wave (middle), and Poisson's ratio (right) perturbations.

200 iterations and produced a variance reduction of at least 90%.

3.2. Resolution and Uncertainty

[20] In order to assess problems associated with our sampling geometry and to verify the resolution of our model we carried out a large number of test inversions with synthetic data, using a range of different input models. Figure 4 shows examples for synthetic models with target anomalies in the upper, middle, and lower mantle. Rays are traced through a known velocity model and then the resulting travel time anomalies are jointly inverted to see what structure is actually recovered for the *P* wave, *S* wave velocity, and Poisson's ratio models. We chose to plot only cells that are crossed by more than two *P* (and *S*) rays; blank cells indicate regions with no resolution. In addition, Figure 3 shows the sampling for the same cross sections and maps as in Figures 4 and 5. Figure 3 indicates that the sampling is irregular in the upper mantle but that the central region blocks are hit by more than 100 rays even in the deepest layers. After inversion the target anomaly location is correctly recovered in areas sampled by rays (Figure 4.). By changing the size of the input anomalies we estimated that the anomaly minimum size that can be recovered is about 800–1000 km. All test results suggest that the magnitude of the actual structures is generally underestimated. For an anomaly of ±5% the anomaly amplitude recovery is about ±4% for both *P* wave and *S* wave

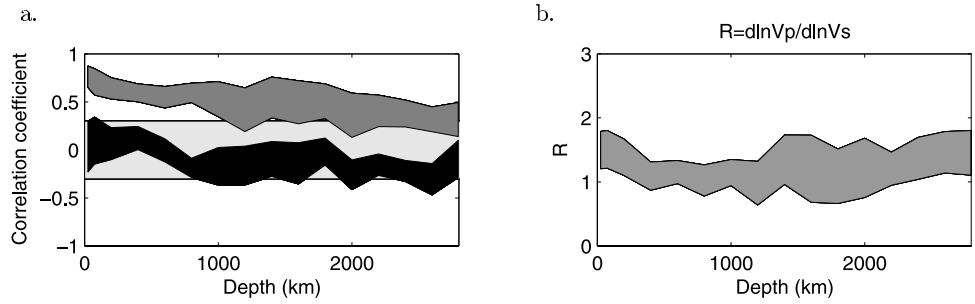

Figure 6. (a) Correlation coefficients for P and S wave velocity models (dark gray) and bulk sound and S wave velocity models (gray). Shaded region (light gray) shows range of correlation coefficients (±0.3) we consider insignificant. (b) Relative variation of P wave and S wave velocity perturbations, $R = \partial \ln v_S / \partial \ln v_P$, as a function of depth.

perturbations at the center of the perturbed area and less at the edges of the anomalies which is partly a consequence of the regularization introduced in the inversion.

[21] Figure 4g shows the recovery of Poisson's ratio with the same input anomaly geometry as in Figures 4a and 4f but with perturbation of opposite sign for P wave and S wave velocity. Note that a velocity perturbation of +5% for P wave velocity and −5% for S wave velocity induces a Poisson ratio perturbation of about 20%. The comparable data coverage and similarity of the regularization effect for the P and S part would suggest that estimating wave speed ratios is more robust than estimating absolute values. However, remaining differences in P and S sampling and data quality influence Poisson's ratio estimates and are the largest source of uncertainty in our results. Instead of selecting a single model we therefore present and draw conclusions from a large number of realizations, produced with different levels of regularization, giving acceptable fits to data (as determined by a χ^2 criterion, with $\chi^2 \approx 1.2$).

4. Results of Inversion for Elastic Parameters

[22] The bulk sound models obtained using equation (2) are virtually indistinguishable from the models obtained from equation (3), confirming conclusions by *Kennett et al.* [1998]. Because it is impossible to represent lateral variations of all the acceptable models, we show lateral variations of one of them. Figures 5a, 5b, and 5c present lateral variations in compressional, shear, and bulk sound wave speed for three depths in the lower mantle. We plotted the parameter estimates for cells that are crossed by at least two rays, but we used equation (5) to calculate the Poisson's ratio (σ) only for blocks sampled by at least four P and S rays (Figure 5d). Despite the much smaller data set used, our results for v_P are in excellent agreement with the global tomographic images of *Kárason and van der Hilst* [2001], who used a large range of data, including *P*, *pP*, *PP*, *PKP*, and P_{diff}, an irregular grid parameterization, and 3-D sensitivity kernels for the low-frequency phases.

[23] In the upper mantle, ray coverage is fairly sparse since it is restricted primarily to blocks directly beneath the sources and stations. Therefore we choose not to interpret the calculated Poisson's ratios in the shallow mantle. Beginning at ~650 km depth, the ray coverage is much denser and coherent patterns begin to emerge. In the top of the lower mantle beneath the Aleutian and Kuril arcs, there are regions of high shear wave speed and low Poisson's ratios in the same locations where global tomography [e.g., *Kárason and van der Hilst*, 2001] and geodynamical modeling [e.g., *Steinberger*, 2000] suggest the presence of slabs of subducted lithosphere. Therefore it seems plausible that at least some of the variability in shear and Poisson's ratio near the top of the lower mantle is due to thermal anomalies associated with slabs subducting in the mantle. These features do not show up as visibly on the bulk sound maps, which concurs with the results of *Widiyantoro et al.* [1999], who noticed that presumed slabs in the lower mantle beneath northwestern Pacific island arcs have a strong signature in rigidity but much less in (in)compressibility.

[24] Behind the Aleutian arc we observe a change in Poisson's ratio from low to high near 1000 km depth. These higher Poisson's ratios persist to ~2000 km depth. In the same area, the bulk sound and shear wave models appear anticorrelated. In the bottom 300 km, above the core-mantle boundary, we infer large regions of low Poisson's ratio and strong positive shear velocity anomaly (suggesting more rigid material) surrounding smaller areas of higher Poisson's ratio and negative shear velocity anomaly (suggesting less rigid material). The value of Poisson's ratio in the central zone is ~0.29, which is similar to but not quite as low as the value found by *Wysession et al.* [1999] from diffracted waves, while the value in the surrounding regions is ~0.31.

[25] In this paper we refrain from a more detailed discussion of the lateral variations depicted in Figure 5. Instead, we focus on the change in depth of (1) the correlation between v_P and v_S and between v_S and v_ϕ, (2) the ratio between relative variations in v_P and v_S, and (3) the Poisson's ratio for the range of acceptable models. On Figure 6 the shaded bands comprise all individual realizations, constructed with different levels of regularization and data noise, that give acceptable fit to the data. Figure 6a shows that the correlation between v_P and v_S decreases (top curve) gradually with increasing depth. Above ~2000 km depth the variations correlate fairly well (correlation coefficient $r > 0.5$), which is in agreement with global inversions of P and S wave data [i.e., *Robertson and Woodhouse*, 1996; *Kennett et al.*, 1998; *Masters et al.*, 2000; *Saltzer et al.*, 2001]. In the bottom 1000 km of the model, however, the correlation coefficient, r, is less than 0.5. There does not seem to be a significant correlation between variations in bulk sound and shear speed (bottom curve) at any depth in the lower mantle beneath our study

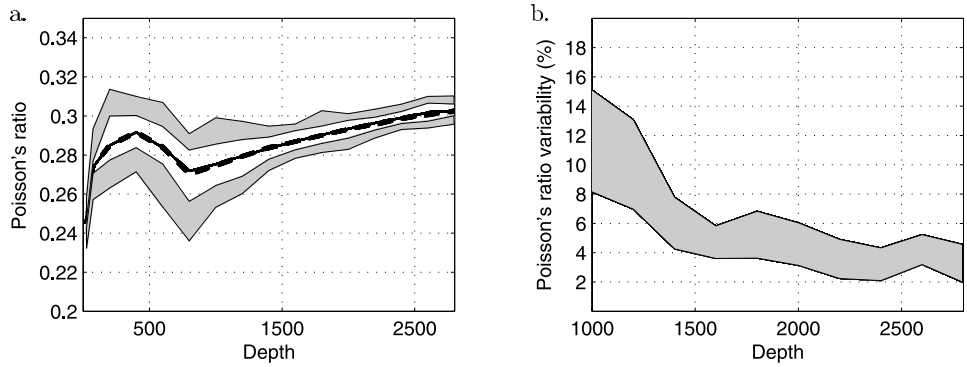

Figure 7. (a) Poisson's ratio as a function of depth for reference model (solid black line), and mean of each layer (dashed black line). The two gray areas represent the minimum and maximum Poisson's ratio of all acceptable models as a function of depth. (b) Plot of Poisson's ratio variability, which is the range between the minimum and maximum Poisson's ratio converted to percent with respect to the average model.

region ($-0.3 < r < 0.3$), but on average, the correlation coefficient may be slightly negative in the lower mantle, especially beneath 2000 km depth. Indeed, in the maps of Figure 5 one can readily identify regions where the variations in bulk and shear are anticorrelated. The low degree of correlation between bulk sound and shear wave speed in the bottom half of the mantle is consistent with global analyses [e.g., *Masters et al.*, 2000; *Saltzer et al.*, 2001].

[26] For our study region the laterally averaged value of $R = R(z) = d\ln V_S/d\ln V_P$ remains well below the high values reported in some global studies (see *Masters et al.* [2000] for a review) and below the values that are thought to imply, unambiguously, compositional heterogeneity: it increases gradually from $\sim$1.0–1.4 at 1000 km depth to $\sim$1.2–1.8 in the bottom 300 km, with substantial scatter (regularization induced) between 1200 and 2000 km depth (Figure 6b).

[27] Figure 7a shows the average Poisson's ratio and the magnitude of its lateral variations as a function of depth. At all depths the average Poisson's ratio value is within a fraction of a percent of the value given by the ak135 reference model. For each of the large number of acceptable models (constructed with different levels of regularization and data noise) we determine the minimum and maximum Poisson's ratio at each depth and plot them has a function of depth (lower and upper gray areas of Figure 7a). The range between the minimum and maximum Poisson's ratio is then converted to percent with respect to the average model and plotted on Figure 7b. The variability in Poissson's ratio decreases rapidly from 8–15% at 1000 km depth to 6–12% at 1250 km and 4–7% at 1500 km, beyond which it gradually decreases to 2–5% in the bottom 500 km (Figure 7b).

5. Effects of Temperature and Composition

[28] For the interpretation of the inferred variability in Poisson's ratio we assume that the lower mantle composition corresponds to a perovskite (pv)-magnesiowüstite (mw) assemblage $\theta(Mg_{1-\alpha}, Fe_{\alpha})SiO_3 + (1 - \theta)(Mg_{1-\beta}, Fe_{\beta})O$. We take initial proportion parameters consistent with a pyrolitic composition, that is, $\theta = 0.7$ and $\alpha = \beta = X_{Fe} = Fe/[Fe + Mg] = 0.1$. To investigate the effects of composition, we consider two possibilities. First, we calculate the effect on Poisson's ratio of a change in X_{Fe}, that is the modal iron content in the pv-mw assemblage. Second, we investigate the effect on Poisson's ratio of changes in, θ, the relative proportion of pv. Since its effect on Poisson's ratio depends on iron content (X_{Fe}) and partitioning (α, β), we also investigate the relationship between these parameters. In this study we do not take into account the effects of minor constituents, such as calcium (which would be present mainly in Ca-pv, $CaSiO_3$) and aluminum (mainly in Mg, Fe pv).

5.1. Effect of Temperature

[29] In order to investigate the effect of temperature on Poisson's ratio we calculated its partial derivative, $\partial\sigma/\partial T$, at various depths using the analysis of *Karki and Stixrude* [1999] for the reference pv-mw assemblage mentioned above. First, v_P and v_S are calculated as a function of pressure for pv and mw, separately, and then extrapolated to lower mantle temperature. Subsequently, we calculate the wave speeds for the assemblage and estimate Poisson's ratio partial derivative by varying the temperature. Following *Karki and Stixrude* [1999], we considered three cases for calculating the effect of iron on the shear modulus of pv (see section 5.2), but we found that they do not change the effect of temperature on Poisson's ratio. Likewise, neither the value of X_{Fe} nor the relation between α and β has a significant influence on the effect of temperature.

[30] Figure 8 illustrates the effect of temperature on Poisson's ratio. For different depths in the lower mantle we first compare the calculated effect of a thermal anomaly of 300 K with the variability in Poisson's ratio inferred from our seismic data (Figure 8a). For two selected depths, 1300 and 2700 km, we then calculate the effect on Poisson's ratio of temperature variation and compare it to the inferred variability for those depths (Figures 8b and 8c). Both for comparison and as an indication of uncertainty in the derivatives we also show the percent change in Poisson's ratio inferred from other temperature-velocity derivatives [*Karato*, 1993; *Stacey*, 1998; *Trampert et al.*, 2001], all of which were derived using third-order Birch-Murnaghan

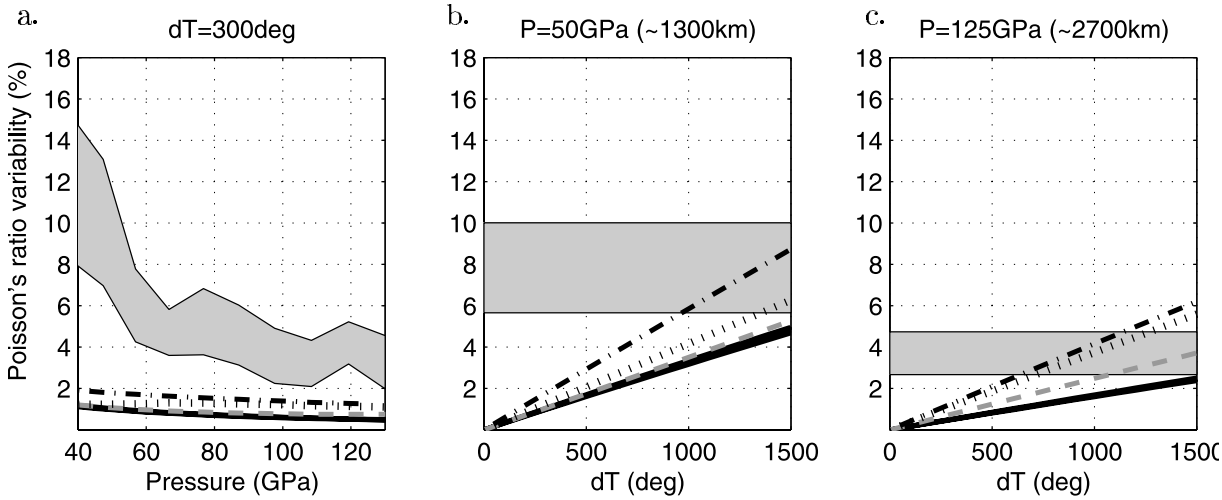

Figure 8. (a) Effect of a 300° thermal anomaly on Poisson's ratio at various pressures. Poisson's ratio perturbation is computed with equation (5) and the temperature-velocity derivatives of *Stacey* [1998] (dash-dotted line), *Karato* [1993] (dotted line), *Trampert et al.* [2001] (gray dashed line), and *Karki and Stixrude* [1999] (black line). For comparison, the gray area shows Poisson's ratio variability inferred from the range of acceptable models (same as Figure 7b except depth axis is converted to pressure). (b) and (c) Effect of various thermal anomalies on Poisson's ratio at a constant pressure of 50 GPa (~1300 km depth) (Figure 8b) and 125 GPa (~2700 km) (Figure 8c) using the same derivatives as in Figure 8a. Gray rectangle of Figures 8b and 8c shows Poisson ratio variability from our models at the given pressures.

equations of state to extrapolate mineral physics data from relatively low pressures to lower mantle conditions. The extrapolations are based on several assumptions and approximations (e.g., quasi-harmonic approximations, higher-order anharmonic terms), and all assumed a simplified model of the lower mantle consisting of pv and mw only. The *Karato* [1993] derivatives include an estimate for the effects of anelasticity, which is adopted here.

[31] Near the base of the mantle (125 GPa, Figure 8c) a given temperature difference has a smaller effect on Poisson's ratio than at shallower depths (e.g., 50 GPa, Figure 8b), but the magnitude of the effect varies by a factor of 2 depending upon which derivative is used. A temperature difference of 300° would yield variability in Poisson's ratio of 1–2% at 1300 km depth and 0.5–1.5% near the CMB. Explaining the minimum peak-to-peak variability in Poisson's ratio entirely in terms of a thermal origin would, depending on which set of derivatives is used, requires temperature differences of 1000–1700 K at 1300 km depth, for derivatives from *Stacey* [1998] and *Karki and Stixrude* [1999], respectively, and of 600–1500 K at the base of the mantle.

5.2. Effect of Iron Content

[32] In order to investigate the effect of iron content on Poisson's ratio we computed its partial derivative, $\partial\sigma/\partial X_{\mathrm{Fe}}$, at various depths using the analysis of *Karki and Stixrude* [1999] for the reference pv-mv assemblage mentioned above.

[33] As before, we first computed v_P and v_S as a function of pressure for mw and pv, separately, and extrapolated them to lower mantle temperatures. Then, we computed the wave speeds for the pv-mw assemblage. The partial derivatives of the Poisson's ratio of the assemblage with respect to iron content were then computed by varying X_{Fe} around the reference value (that is, $X_{\mathrm{Fe}} = 0.1$). The effect of changes in iron content, X_{Fe}, on the elastic moduli of pv and mw is not well known, and therefore we had to consider different hypotheses.

[34] Experiments have shown that the effect X_{Fe} on the bulk modulus is negligible [*Mao et al.*, 1991; *Fei et al.*, 1992]. Therefore we did not vary that parameter for either mineral.

[35] Experimental results [*Duffy and Anderson*, 1989] show that for mw the rigidity decreases with increasing X_{Fe} according to

$$\mu = \mu_0(1 - 0.59X_{\mathrm{Fe}}), \tag{6}$$

with μ_0 the shear modulus for $X_{\mathrm{Fe}} = 0$.

[36] There are no such constraints on the effect on the pv shear modulus. Following *Karki and Stixrude* [1999], we consider three possibilities. First, iron has no effect on pv shear modulus, so the only change to the pv velocities results from the effect of iron on density, which we calculate following *Jeanloz and Thompson* [1983]. Second, the effect of iron on the pv shear modulus is similar to that observed in orthopyroxene [*Duffy and Anderson*, 1989]. Third, the effect of iron is the same as that observed for mw [*Duffy and Anderson*, 1989]; see equation (6).

[37] We have calculated partial derivatives of the Poisson's ratio with respect to iron content for our reference pv-mw assemblage considering each of the three dependencies of rigidity on changes in iron mentioned above. Figure 9 shows the computed effect of a change in X_{Fe} on the Poisson's ratio for these three cases: (1) pv shear modulus is unaffected by iron (dashed curves), (2) pv shear modulus is affected similarly to mw (dash-dotted curves);

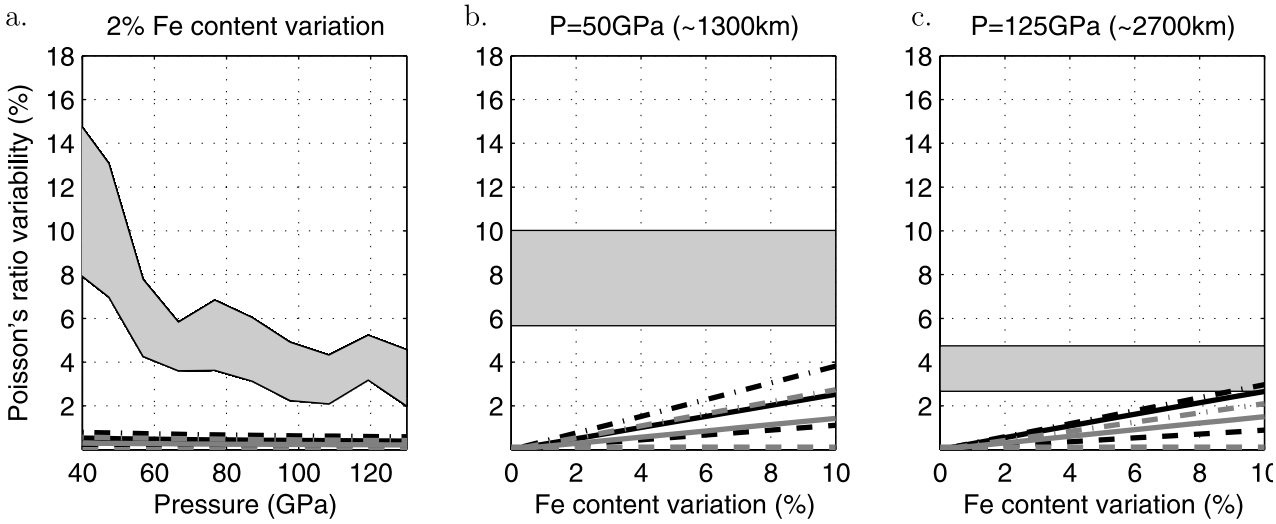

Figure 9. Effect of iron content variation on Poisson's ratio variability at various pressures. (a) Effect of a 2% iron content variation as a function of pressure. (b) and (c) Effect of different amounts of iron enrichment/depletion at pressures of 50 GPa (~1300 km depth) and 125 GPa (2700 km). We use the iron content-velocity derivatives of *Karki and Stixrude* [1999] in a lower mantle made of 70% perovskite (pv) and 30% magnesiowüstite (mw) with 10% of iron. Black curves correspond to the case in which iron is equally partitioned between pv and mw, and gray curves correspond to when all the iron is in pv. As the effect of iron on pv shear modulus is unknown, we consider three different behavioral effects of the pv shear modulus: (1) pv shear modulus is unaffected by iron (dashed black curve), (2) pv shear modulus is affected similarly to mw (dash-dotted curve); and (3) pv shear modulus is affected similarly to orthopyroxene (gray solid line). For comparison, the gray areas show Poisson's ratio variability inferred from the range of acceptable models (same as Figure 8).

(3) pv shear modulus is affected similarly to orthopyroxene (solid lines). For each of these cases, we have considered either that iron is equally partitioned between pv and mw (black curves, $\alpha = \beta$) or that all the iron is in pv (gray curves, $\beta = 0$). For the hypothesis yielding the largest sensitivity, i.e., case 2, the shear modulus in pv behaving like that of mw and equal partition of iron between pv and mw, a 1% variability in Poisson's ratio can be explained by a relative change in X_{Fe} of 2% (Figures 9b and 9c). If the observed magnitude of the variations in σ were to be explained entirely by variations in Fe content alone, a change of $\Delta X_{Fe} = 16\%$ would be required at 1000 km depth and $\Delta X_{Fe} = 8\%$ at the base of the mantle. In the case that all the iron is in pv, the iron content variation would be slightly larger, that is 19% and 11% respectively. For the other two hypotheses on pv shear modulus behavior, the derivatives are smaller so that even larger variations in iron content would be implied.

5.3. Effect of Partitioning Between Perovskite and Magnesiowüstite

[38] Investigating the effect of a change in pv proportion in the pv-mw assemblage is complicated because the relative velocities are affected by the presence of iron. Moreover, the total amount of iron in the lower mantle is debated, and there are discrepancies between experimental results on iron partitioning between the two minerals. Consequently, for the assemblage $\theta(Mg_{1-\alpha}, Fe_{\alpha})SiO_3 + (1 - \theta)(Mg_{1-\beta}, Fe_{\beta})O$, where θ is the pv proportion, the value of α and the relation between α and β are not well constrained. Many studies suggest that iron tends to concentrate in the mw ($\alpha \approx 0$) [*Yagi et al.*, 1997; *Ito et al.*, 1984; *Guyot et al.*, 1988; *Ito and Takahashi*, 1989; *Mao et al.*, 1997], in particular if there is a transition from high spin to low spin [*Badro et al.*, 2003]. Others have suggested that the partitioning may be more equal ($\alpha \approx \beta$) [*Wood and Rubie*, 1996; *Kesson et al.*, 1998], and with the inclusion of aluminum in the mix the iron may actually concentrate entirely in the pv ($\beta \approx 0$) [*McCammon*, 1997].

[39] Bearing these experimental uncertainties in mind, we calculated Poisson's ratio partial derivatives with respect to θ for these three extreme cases and different percentage of iron in the lower mantle. We find that a change in the θ does not really affect Poisson's ratio in any significant manner unless (1) there is a significant amount of iron in the lower mantle ($X_{Fe} > 0.1$), (2) all of that iron partitions exclusively into either the mw ($\alpha \approx 0$) or the pv minerals ($\beta \approx 0$), (3) the shear modulus is strongly effected by the addition of iron, and (4) the bulk modulus is unaffected by the presence of iron. If those criteria are met, a change in the relative amount of pv may explain part of the inferred variability in Poisson ratio.

[40] Figure 10 shows the effect of the relative amount of pv using the *Karki and Stixrude* [1999] derivative when all the iron (10%) is in the pv (i.e., $\alpha = 0.1$, $\beta = 0$). For comparison, we also use the formulation by *Trampert et al.* [2001] (solid black line). The two differ on the magnitude of the effect. The *Karki and Stixrude* [1999] derivatives show that a 20% difference in the volume proportion of pv would, at most, give rise to ~1.% variability in Poisson's ratio at ~1300 km depth (50 GPa) and ~0.8% at the base of the mantle (Figure 9). Using the derivatives from *Trampert et*

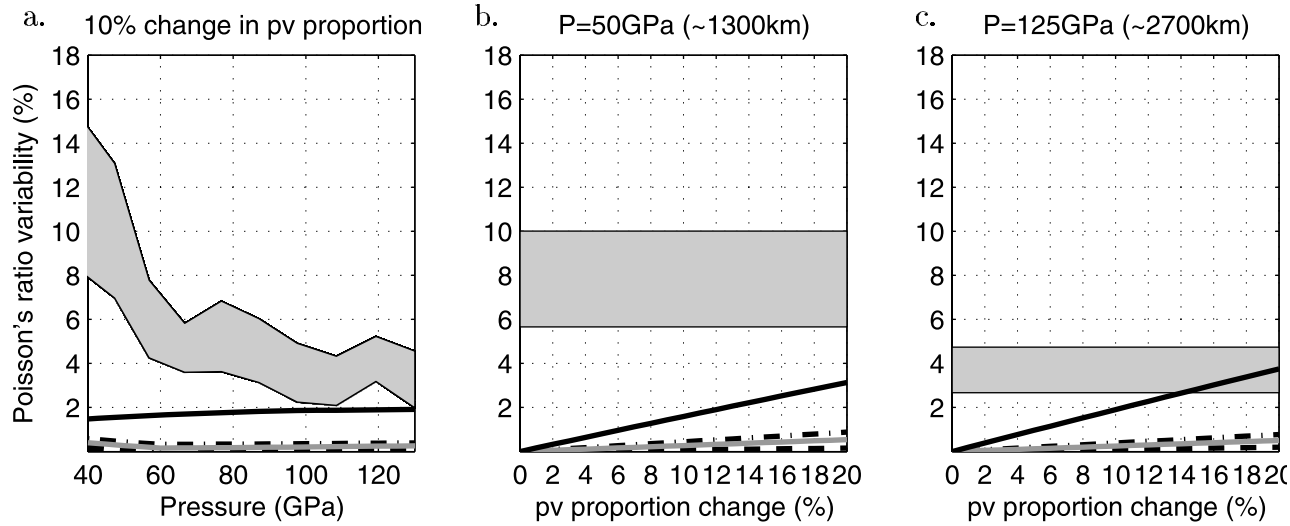

Figure 10. Effect of change in $MgSiO_3$ proportion on Poisson's ratio at various pressures. (a) Effect on Poisson's ratio variability of a 10% variation of $MgSiO_3$ proportion at various pressures. (b) and (c) Effect of different amounts of perovskite (pv) enrichment/depletion at depths of 1300 km (Figure 10b) and at 2700 km depth (Figure 10c). We use the compositional-velocity derivatives of *Trampert et al.* [2001] (solid black line) and *Karki and Stixrude* [1999] (black dashed, black dash-dotted and solid gray lines). Using the derivative from *Karki and Stixrude* [1999], we consider a lower mantle made of 70% pv and 30% magnesiowüstite (mw) with $\alpha = 0.1$ and $\beta = 0$. As the effect of iron on pv shear modulus is unknown, we consider three different behavioral effects of the pv shear modulus: (1) pv shear modulus is unaffected by iron (dashed black curve), (2) pv shear modulus is affected similarly to mw (dash-dotted curve); and (3) pv shear modulus is affected similarly to orthopyroxene (gray solid line). For comparison, the gray areas show Poisson's ratio variability inferred from the range of acceptable models (same as Figure 8).

al. [2001], this same variability can be explained by a much smaller difference in volume proportion of pv. We note, however, that their compositional derivatives do not come with a clear statement of how iron was partitioned between the two minerals nor what assumptions were made concerning the effect of iron on the shear and bulk moduli, which makes it difficult to assess the differences between these two sets of predictions. Recognizing the inherent uncertainties in both methods, these derivatives show that 10% perovskite depletion (or enrichment) can explain about one tenth to one third of the minimum variability in Poisson's ratio that we see at 1000 km depth and between one to four fifth of the variability at the base of the mantle.

6. Discussion

[41] The thermal anomalies required to explain the inferred variability in Poisson's ratio vary depending on which set of partial derivatives are used. However, even with the largest sensitivities considered here [*Stacey*, 1998] one would need lateral variations in temperature between ~1000 and 1700 K to explain the large range of inferred ratios in the middle mantle and between ~600 to 1200 K near the base of the mantle (Figure 8). Put differently, explaining just the minimum variability in Poisson's ratio requires 1000–1500 K for the middle mantle and 700–1500 K at the bottom of the mantle, depending on the derivatives used. In theory it is possible to explain the inferred variation in Poisson's ratio with a thermal origin, but the occurrence of such large temperature contrasts across a small region is not plausible.

[42] There is no tomographic evidence of subduction deeper than about 1000 km beneath the central part of our region, but let us assume that slabs fragments do exist there (Figure 1b). A simple heat diffusion calculation shows that away from the thermal boundary layers, the thermal anomalies associated with cold slabs are likely to be of the order of 300–400 K (Table 1). Figure 8 shows, however, that an anomaly of ~400 K would only explain a fraction of the inferred variability in Poisson's ratio.

Table 1. Values Used in Slab Temperature Calculation[a]

	Length of Time Spent, Myr	ρ, kg/m^3	Ambient Mantle Temperature, °C	κ, W/mK
Upper mantle	17	3400	1350	4.5
Top of lower mantle	40	4000	1800	7.0
Bottom of lower mantle	40	5500	2700	9.6
D″	20	5600	3450	10.0

[a]In the diffusion equation we use the specific heat Cp = 1250 (J/Kg K) at all depths, slab thickness is 100 km, and temperature profile increases linearly from 200° to 1200°C.

[43] Let us further assume that part of the Poisson's ratio variability in the region could be due hot material associated with hitherto undetected plumes. The amplitude of the associated excess temperature is not likely to exceed ~300 K [e.g., *Sleep*, 1988; *Farnetani*, 1997], so that even if hot plumes and cold slab fragments coexisted in the relatively small region under study, the total thermal anomaly amplitude would be no more than ~700 K. At 1300 km depth such a thermal perturbation would yield a variability in Poisson's ration of ~2–4%, which is still much less than the inferred range at that depth; just above the CMB the predicted scatter in Poisson's ration could be 1.0–2.5%, which, again, is well below the level inferred from the data. So even in this extreme case, the thermal effect alone is still far from explaining the inferred Poisson's ratio variability.

[44] Because no plausible thermal anomalies seem able to explain the seismological observations, we explored the effects of lateral variations in major element composition. A variation of the iron content can explain part of the Poisson's ratio variability, but the derivatives used here suggest that we can explain at most 1% change in Poisson's ratio for each 2% change in the X_{Fe}. Investigating the effect of a change in pv proportion, i.e., θ, is more complex because it depends strongly on the iron content and on the iron partitioning between pv and mw. If the lower mantle is composed of 70% pv and 30% mw, i.e., $\theta = 0.7$, and if all iron is partitioned either in pv or in mw, then a 10% change in pv content could explain one half to four fifths of the inferred Poisson ratio variability if we use the partial derivative derived from *Karki and Stixrude* [1999]. The *Trampert et al.* [2001] compositional derivatives suggest larger effects, but the role of iron is not specified.

[45] Along with the observed anticorrelation of bulk and shear wave speed, the above considerations suggest that no reasonable temperature anomaly can, by itself, explain the Poisson's ratios and that thus a combination of changes in temperature, iron content, and pv versus mw proportion must be involved. Furthermore, the combinations of temperature variations and compositional effects considered here are barely capable of explaining the large variability in Poisson's ratio. This might suggest that there are more effects. One effect could be anelasticity. Its importance is still debated [e.g., *Trampert et al.*, 2001], but we cannot rule out that the effects are larger than accounted for here. Another influence could be the presence of minor constituents, such as Ca and Al. These effects are not investigated in this paper because of the large uncertainties on these parameters.

[46] It is interesting to note that our estimates of the ratio $R = \partial \ln v_S / \partial \ln v_P$ do not signal the need for compositional heterogeneity. Indeed, R remains well below the high values reported in some global studies (see *Masters et al.* [2000] for a review) and below the values that are thought to imply, unambiguously, compositional heterogeneity. We must realize, however, that because of the way it is determined, R typically represents an average over a large area. We recall that also the layer averages of Poisson's ratio (Figure 7a) are close to global reference values, whereas the lateral variability exceeds what can be explained by a thermal origin alone. These observations suggest (1) that compositional heterogeneity cannot, in general, be ruled out if R is smaller than certain critical values and (2) that lateral variability and not a layer average is the relevant diagnostic value.

7. Conclusions

[47] By means of waveform cross correlation we have measured ~17,000 P and S wave differential travel times from earthquakes and receivers near a great circle path from Japan, across Alaska, to western North America. We inverted these data for determining high-resolution tomographic models of P wave, S wave, and bulk sound speeds. We explored the model space using different levels of regularization and our conclusions are based on a range of models that give acceptable data fits (χ^2).

[48] The correlation between variations in v_S and v_P is good to ~1500 km depth but gradually degrades in the bottom 1000 km, whereas the relative ratio of relative variations in v_S and v_P is between 1.5 and 2.0 at most depths. Our data suggest that in much of the lower mantle beneath the region of our interest the correlation between bulk and shear wave speed tends to be negative, in particular beneath 2000 km depth. The layer averages may not be statistically significant, but several regions of conspicuous anticorrelation are readily identified.

[49] From the tomographic images we have derived the variability in Poisson's ratio from the surface to the core-mantle boundary for the range of acceptable models. We infer lateral variability in Poisson's ratio of 8–15% at depths of 1000 km, 4–6% at depths of 1500 km, and 2–5% at the bottom of the mantle. We have interpreted these numbers in terms of temperature and compositional effects. At all depths the effect of temperature is largest, and that of pv and mw ratio smallest. Our data cannot resolve the trade-off between thermal and compositional effects, but explaining the inferred variability in Poisson's ratio by temperature alone would require unrealistic perturbations and it would not explain the inferred anticorrelation between shear and bulk sound speed. Our results suggest that a combination of thermal and compositional effects is needed to explain the inferred elastic parameters in the entire depth range of our study, that is the mantle beneath 1000 km. Specifically, a ΔT of ~300–800 K, variation in X_{Fe} of ~4%, and pv enrichment (or depletion) of up to ~10% can explain the large variability in Poisson's ratio in the deep mantle, but only just.

[50] The inferred composition variations are strongly dependent on the effect of iron which is still relatively unknown. Keeping this uncertainty in mind, our results might suggest that there are other effects such as maybe anelasticity. Another influence could be the presence of minor constituents, such as Ca and Al. As additional high-pressure and high-temperature laboratory experiment become available, it will become possible to investigate more precisely the mantle composition variation.

[51] Finally, our results suggest that $R = R(z) = \partial \ln v_S / \partial \ln v_P$ does not unequivocally signal the need for compositional heterogeneity: values larger than, say, 2.5 probably require compositional effects, but smaller values may not necessarily exclude them. Moreover, even when layer averages of R and Poisson's ratio appear consistent with compositionally homogeneous reference models, lateral variability may well

exceed what can be explained by thermal perturbations alone.

[52] **Acknowledgments.** We thank H. Kárason, who generously provided both ray tracing and inversion code; B. Hager, R. O'Connell, and A. Davaille for discussions on the thermal structure of the mantle; and J. Matas for discussions on mineralogy. This research was supported by the National Science Foundation under grant EAR-9905779, the David and Lucille Packard Foundation, and the Institut de Physique du Globe de Paris contribution 1975.

References

Aki, K., and P. Richards (1980), *Quantitative Seismology: Theory and Method*, vol. 1, W. H. Freeman, New York.

Albarède, F., and R. D. van der Hilst (2002), Zoned mantle convection, *Philos. Trans. R. Soc. London, Ser. A*, *360*, 2569–2592.

Anderson, D. L. (2002), The case for irreversible chemical stratification of the mantle, *Int. Geol. Rev.*, *44*, 97–116.

Antolik, M., Y. Gu, G. Ekström, and A. Dziewonski (2003), J362D28: A new joint model of compressional and shear velocity in the Earth's mantle, *Geophys. J. Int.*, *153*, 443–466.

Badro, J., G. Fiquet, F. Guyot, J. P. Rueff, V. V. Struzhkin, G. Vanko, and G. Monaco (2003), Iron partitioning in Earth's mantle: Toward a deep lower mantle discontinuity, *Science*, *300*, 789–791.

Becker, T. W., J. B. Kellogg, and R. J. O'Connell (1999), Thermal constraints on the survival of primitive blobs in the lower mantle, *Earth Planet Sci., Lett.*, *171*, 351–365.

Bijwaard, H., W. Spakman, and E. R. Engdahl (1998), Closing the gap between regional and global traveltime tomography, *J. Geophys. Res.*, *103*, 30,055–30,078.

Castle, J. C., and R. D. van der Hilst (2000), The core-mantle boundary under the Gulf of Alaska: No ULVZ for shear waves, *Earth Planet. Sci. Lett.*, *176*, 311–321.

Coltice, N., and Y. Ricard (1999), Geochemical observations and one layer mantle convection, *Earth Planet. Sci., Lett.*, *174*, 125–137.

Dahlen, F., S. Hung, and G. Nolet (2000), Frechet kernels for finite-frequency traveltimes: I. Theory, *Geophys. J. Int.*, *141*, 157–174.

Davaille, A. (1999), Simultaneous generation of hotspots and superswells by convection in a heterogeneous planetary mantle, *Nature*, *402*, 756–760.

Davis, G. (2002), Stirring geochemistry in mantle convection models with stiff plates and slabs, *Geochim. Cosmochim. Acta*, *66*, 3125–3142.

Duffy, T. S., and D. L. Anderson (1989), Seismic velocities in mantle minerals and the mineralogy of the upper mantle, *J. Geophys. Res.*, *94*, 1895–1912.

Dziewonski, A. M., and D. L. Anderson (1981), Preliminary reference Earth model, *Phys. Earth Planet. Inter.*, *25*, 297–356.

Engdahl, E. R., R. D. van der Hilst, and R. Buland (1998), Global teleseismic earthquake relocation with improved travel times and procedures for depth determination, *Bull. Seismol. Soc. Am.*, *88*, 722–743.

Farnetani, C. (1997), Excess temperatures of mantle plumes: The role of chemical stratification across D″, *Geophys. Res. Lett.*, *24*, 1583–1586.

Fei, Y., H. K. Mao, J. Shu, and J. Hu (1992), P-V-T equation of state of magnesiowüstite ($Mg_{0.6}Fe_{0.4}O$), *Phys. Chem. Miner.*, *18*, 416–422.

Forte, A., and J. Mitrovika (2001), Deep mantle high viscosity flow and thermochemichal structure inferred from seismic and geodynamic data, *Nature*, *410*, 1049–1056.

Forte, A., J. Mitrovika, and A. Espesset (2002), Geodynamic and seismic constrints on the thermochemical structure and dynamics of convection in the deep mantle, *Philos. Trans. R. Soc. London, Ser. A*, *360*, 2521–2543.

Garnero, E. J. (2000), Lower mantle heterogeneity, *Annu. Rev. Earth Planet. Sci.*, *28*, 509–537.

Garnero, E. J., and D. V. Helmberger (1998), Further constraints and uncertainties in modeling a thin varying ultralow velocity layer at the base of the mantle, *J. Geophys. Res.*, *103*, 12,495–12,509.

Grand, S. P., R. D. van der Hilst, and S. Widiyantoro (1997), Global seismic tomography: A snapshot of convection in the Earth, *GSA Today*, *7*, 1–7.

Guyot, F., M. Madon, J. Peyronneau, and J. P. Poirier (1988), X-ray microanalysis of high-pressure/high-temperature phases synthesized from natural olivine in a diamond-anvil cell, *Earth Planet. Sci. Lett.*, *90*, 52–64.

Helffrich, G., and B. Wood (2001), The Earth's mantle, *Nature*, *412*, 501–507.

Hofmann, A. (1997), Mantle geochemistry: The message from oceanic volcanism, *Nature*, *385*, 219–229.

Ishii, M., and J. Tromp (1999), Normal-mode and free-air gravity constraints on lateral variations in velocity and density of Earth's mantle, *Science*, *285*, 1231–1236.

Ishii, M., and J. Tromp (2001), Even degree lateral variations in the Earth mantle constrained by free oscillations and the free-air gravity anomaly, *Geophys. J. Int.*, *145*, 77–96.

Ito, E., and E. Takahashi (1989), Post-spinel transformations in the system Mg_2SiO_4-Fe_2SiO_4 and some geophysical implications, *J. Geophys. Res.*, *94*, 10,637–10,646.

Ito, E., E. Takahashi, and Y. Matsui (1984), The mineralogy and chemistry of the lower mantle: An implication of he ultrahigh-pressure phase relations in the system MgO-FeO-SiO_2, *Earth Planet. Sci. Lett.*, *67*, 238–248.

Jeanloz, R., and B. Thompson (1983), Phase transition and mantle discontinuities, *Rev. Geophys.*, *21*(1), 51–74.

Kárason, H., and R. D. van der Hilst (2001), Tomographic imaging of the lowermost mantle with differential times of refracted and diffracted core phases (*PKP*, P_{diff}), *J. Geophys. Res.*, *106*, 6569–6588.

Karato, S. (1993), Importance of anelasticity in the interpretation of seismic tomography, *Geophys. Res. Lett.*, *20*, 1623–1626.

Karki, B. B., and L. Stixrude (1999), Seismic velocities of major silicate and oxide phases of the lower mantle, *J. Geophys. Res.*, *104*, 13,025–13,033.

Kellogg, L. H., B. H. Hager, and R. D. van der Hilst (1999), Compositional stratification in the deep mantle, *Science*, *283*, 1881–1884.

Kennett, B. L. N., and O. Gudmundsson (1996), Ellipticity corrections for seismic phases, *Geophys. J. Int.*, *127*, 40–48.

Kennett, B. L. N., E. R. Engdahl, and R. Buland (1995), Constraints on seismic velocities in the Earth from traveltimes, *Geophys, J. Int.*, *122*, 108–124.

Kennett, B. L. N., S. Widiyantoro, and R. D. van der Hilst (1998), Joint seismic tomography for bulk sound and shear wave speed in the Earth's mantle, *J. Geophys. Res.*, *103*, 12,469–12,493.

Kesson, S. E., J. D. Fitzgerald, and J. Shelley (1998), Mineralogy and dynamics of a pyrolite lower mantle, *Nature*, *393*, 252–255.

Li, X. D., and B. Romanowicz (1996), Global mantle shear velocity model developed using nonlinear asymptotic coupling theory, *J. Geophys. Res.*, *101*, 22,245–22,272.

Mao, H. K., R. J. Henley, Y. Fei, J. F. Shu, C. Chen, A. P. Jephcoat, Y. Wu, and W. A. Bassett (1991), Effect of pressure, temperature, and composition on lattice parameters and density of (Fe, Mg)SiO_3-perovskites to 30 GPa, *J. Geophys. Res.*, *96*, 1069–1079.

Mao, H. K., G. Shen, and R. J. Hemley (1997), Multivariable dependence of Fe-Mg partitioning in the lower mantle, *Science*, *278*, 2098–2100.

Masters, G., S. Johnson, G. Laske, and H. Bolton (1996), A shear-velocity model of the mantle, *Philos. Trans. R. Soc. London, Ser. A*, *354*, 1385–1411.

Masters, G., G. Laske, H. Bolton, and A. Dziewonski (2000), The relative behavior of shear velocity, bulk sound speed, and compressional velocity in the mantle: Implications for chemical and thermal structure, in *Earth's Deep Interior: Mineral Physics and Tomography From the Atomic to the Global Scale*, *Geophys. Monogr. Ser.*, vol. 117, edited by S. Karato et al., pp. 63–87, AGU, Washington, D. C.

Matzel, E., N. K. Sen, and S. P. Grand (1996), Evidence for anisotropy in the deep mantle beneath Alaska, *Geophys. Res. Lett.*, *23*, 2417–2420.

McCammon, C. (1997), Perovskite as a possible sink for ferric iron in the lower mantle, *Nature*, *387*, 694–696.

Nolet, G. (1985), Solving or resolving inadequate and noisy tomographic systems, *J. Comput. Phys.*, *61*, 463–482.

Paige, C. C., and M. A. Saunders (1982), LSQR: An algorithm for sparse linear equations and sparse least squares, *Trans. Math. Software*, *8*, 43–71.

Persh, S. E., J. E. Vidale, and P. S. Earle (2001), Absence of short-period ULVZ precursors to *PcP* and *ScS* from two regions of the CMB, *Geophys. Res. Lett.*, *28*, 387–390.

Resovsky, J. S., and M. H. Ritzwoller (1999), Regularization uncertainty in density models estimated from normal mode data, *Geophys. Res. Lett.*, *26*, 2319–2322.

Revenaugh, J. S., and R. Meyer (1997), Seismic evidence of partial melt within a possibly ubiquitous low-velocity layer at the base of the mantle, *Science*, *277*, 670–673.

Richards, M. A., B. H. Hager, and N. H. Sleep (1988), Dynamically supported geoid highs over hotspots: Observations and theory, *J. Geophys. Res.*, *93*, 7690–7708.

Ritsema, J., and H. van Heijst (2002), New constraints on the P velocity structure of the mantle from *P*, *PP*, *PPP*, and *PKPab* travel-times, *Geophys. J. Int.*, *149*, 482–489.

Robertson, G. S., and J. H. Woodhouse (1996), Ratio of relative *S* to *P* velocity heterogeneity in the lower mantle, *J. Geophys. Res.*, *101*, 20,041–20,052.

Romanowicz, B. (2001), Can we resolve 3D density heterogeneity in the lower mantle?, *Geophys. Res. Lett.*, *28*, 1107–1110.

Saltzer, R. L., R. D. van der Hilst, and H. Kárason (2001), Comparing *P* and *S* wave heterogeneity in the mantle, *Geophys. Res. Lett.*, *28*, 1335–1338.

Sleep, N. (1988), Gradual entrainment of a chemical layer at the base of the mantle by overlaying convection, *Geophys. J.*, *95*, 437–447.

Stacey, F. D. (1998), Thermoelasticity of a mineral composite and a reconsideration of lower mantle properties, *Phys. Earth Planet. Inter.*, *106*, 219–236.

Steinberger, B. (2000), Slabs in the lower mantle-results of dynamic modeling compared with tomographic images and the geoid, *Phys. Earth Planet. Inter.*, *118*, 241–257.

Su, W., and A. M. Dziewonski (1997), Simultaneous inversion for 3-D variations in shear and bulk velocity in the mantle, *Phys. Earth Planet. Inter.*, *100*, 135–156.

Tackley, P. J. (1998), Three-dimensional simulations of mantle convection with a thermo-chemical basal boundary layer: D"?, in *The Core-Mantle Boundary Region*, *Geodyn. Ser.*, vol. 28, edited by M. Gurnis et al., pp. 231–253, AGU, Washington, D. C.

Trampert, J., P. Vacher, and N. Vlaar (2001), Sensitivities of seismic velocities to temperature, pressure and composition in the lower mantle, *Phys. Earth Planet. Inter.*, *124*, 255–267.

van der Hilst, R. D., and H. Kárason (1999), Compositional heterogeneity in the bottom 1000 kilometers of Earth's mantle: Toward a hybrid convection model, *Science*, *283*, 1885–1888.

van der Hilst, R. D., S. Widiyantoro, and E. R. Engdahl (1997), Evidence for deep mantle circulation from global tomography, *Nature*, *386*, 578–584.

Widiyantoro, S., B. L. N. Kennett, and R. D. van der Hilst (1999), Seismic tomography with P and S data reveals lateral variations in the rigidity of slabs, *Earth Planet. Sci. Lett.*, *173*, 91–100.

Wood, B. J., and D. C. Rubie (1996), The effect of alumina on phase transformations at the 660 km discontinuity from Fe-Mg partition experiments, *Science*, *273*, 1522–1524.

Wysession, M. E., E. A. Okal, and C. R. Bina (1992), The structure of the core-mantle boundary from diffracted waves, *J. Geophys. Res.*, *97*, 8749–8764.

Wysession, M. E., A. Langenhorst, M. J. Fouch, K. M. Fischer, and I. Ghassan (1999), Lateral variations in compressional/shear velocities at the base of the mantle, *Science*, *284*, 120–125.

Yagi, T., P. M. Bell, and H. K. Mao (1997), Phase relations in the system MgO-FeO-SiO2 between 150 and 700 kbars at 1000°C, *Year Book Carnegie Inst. Washington*, *78*, 614–618.

Zindler, A., and S. Hart (1986), Chemical geodyanmics, *Annu. Rev. Earth Planet. Sci.*, *14*, 493–571.

R. L. Saltzer, ExxonMobil Upstream Research, 3319 Mercer Street, Houston, TX 77027, USA. (rsaltzer@alum.mit.edu)

E. Stutzmann, Institut Physique du Globe, 4 Place Jussieu, F-75232 Paris, France. (stutz@ipgp.jussieu.fr)

R. D. van der Hilst, Department of Earth, Atmospheric and Planetary Sciences, Massachusetts Institute of Technology, Room 54-514, Cambridge, MA 02139, USA. (hilst@mit.edu)